Chemical Science

ROYAL SOCIETY OF CHEMISTRY

EDGE ARTICLE

View Article Online
View Journal | View Issue

Cite this: *Chem. Sci.*, 2026, **17**, 6099

All publication charges for this article have been paid for by the Royal Society of Chemistry

Received 29th November 2025
Accepted 26th January 2026

DOI: 10.1039/d5sc09343k

rsc.li/chemical-science

Cobalt-mediated structural transition: facilitating rapid synthesis and enhanced performance of pyrochlore materials for efficient water electrolysis

Yanzong Huang,[ab] Tongtong Liu,[ab] Qingren Zhang,[ab] Yanfei Wang,*[c] Zhengping Zhang *[ab] and Feng Wang *[ab]

Vacancies, which inevitably exist in all solids, influence numerous atomic behaviors and material properties and play a crucial role in both synthesis processes and application performance. In this study, we present a successful approach utilizing the flexible transition between [CoO_4] and [CoO_6] polyhedra to modulate the oxygen vacancies for further controlling the formation of ruthenate pyrochlores and enhancing the electrocatalytic performance for the oxygen evolution reaction. During the formation of the pyrochlore phase, the incorporation of [CoO_4] tetrahedra introduces an inherent oxygen deficiency, accompanied by the beneficial transformation of [CoO_4] tetrahedra into [CoO_6] octahedra. It kinetically accelerates the diffusive reaction rate constant by 164 times. On the other hand, during the oxygen evolution process by the lattice oxygen mediated mechanism, the flexible transformation between [CoO_6] octahedra and [CoO_4] tetrahedra in pyrochlores can effectively mitigate lattice distortions and suppress the metal–insulator transition induced by atomic rearrangements, thereby significantly enhancing the service life of this multicomponent electrocatalyst in proton and anion exchange membrane water electrolysis applications.

Introduction

Vacancies, as a type of structural defect characterized by the absence of lattice atoms, play a pivotal role in facilitating atomic migration, expediting diffusive phase transitions and structural reconfigurations, and influencing various material properties.[1–3] Although this point defect cannot be entirely eliminated in any solid due to increased entropy, its presence is also constrained by the thermodynamic equilibrium, and once the equilibrium is broken, structural damage may occur uncontrollably. As a representative example, the lattice oxygen-mediated mechanism (LOM) in the oxygen evolution reaction (OER) relies on oxygen vacancies (O_v).[4,5] These vacancies not only facilitate lattice oxygen diffusion during the redox process of lattice oxygen in the OER, but also serve as electron trapping and releasing centers, thereby influencing the electron transfer kinetics of catalysts.[6–9] However, the lower energy barrier and faster kinetics resulting from oxygen vacancies also pose a significant challenge due to the uncontrollable increase in oxygen vacancies. This may lead to structural collapse, such as in RuO_2, or induce metal–insulator (M–I) transitions driven by alterations in the lattice field, as observed in ruthenate pyrochlores and iridate perovskites.[10,11] In both scenarios, these issues will result in a sharp decline in the electrocatalytic OER performance. Therefore, it is crucial to create oxygen vacancies that are abundant yet structurally stable for the performance modulation of these significant materials in water electrolysis and hydrogen production applications.

As one of the critical factors, the stability of oxygen vacancies in metal oxides is primarily determined by the oxygen states within [MO_x] configurations.[5,12,13] Generally, the [MO_x] configurations exhibit relatively high stability, which is attributed to the coordination field effects arising from the electronic structure of metal cations.[14] Among the various metal elements, cobalt (Co), as a notable exception, has attracted considerable attention owing to its unique electronic structure and coordination configurations. Specifically, cobalt can adopt polyhedral geometries with distinct configurations, such as the high-spin Co^{2+} ($e_g^4t_{2g}^3$) state in [CoO_4] tetrahedra characterized by high binding energy or the low-spin Co^{3+} ($t_{2g}^6e_g^0$) state in [CoO_6] octahedra associated with low binding energy.[15–17] It is challenging to observe the unitary valence state of Co^{2+} or Co^{3+} in steady-state oxides (*i.e.*, Co_3O_4). Additionally, this phenomenon indicates that the highly adaptable [CoO_x] units can be readily distorted into either oxygen-deficient [CoO_4] tetrahedra or

[a]*State Key Laboratory of Chemical Resource Engineering, Beijing Key Laboratory of Electrochemical Process and Technology for Materials, Beijing University of Chemical Technology, Beijing 100029, P. R. China. E-mail: zhangzhengping@mail.buct.edu.cn; wangf@mail.buct.edu.cn*

[b]*National Engineering Research Center for Fuel Cell and Hydrogen Source Technology, Beijing University of Chemical Technology, Beijing 100029, P. R. China*

[c]*Petrochina Petrochemical Research Institute, Beijing 102206, P. R. China. E-mail: wangyanfei010@petrochina.com.cn*

oxygen-rich [CoO_6] octahedra in response to external conditions, both of which exhibit structural stability.[18–21] Therefore, we propose a method for generating enhanced and stabilized oxygen vacancies by incorporating Co elements into ruthenate pyrochlores for OER electrocatalysis. The impact of introduced Co elements and the potential formation of oxygen vacancies on material behavior were thoroughly investigated, involving the phase transition into pyrochlore structures and electrochemical performance, in consideration of the defect effect on atomic migration and physical properties.

Results and discussion

To ensure the homogeneous dispersion of each component in the precursors of ruthenate pyrochlores, the sol–gel self-propagating method was employed to achieve forced blending.[22–24] As shown in Fig. S1, the precursor powders of pristine yttrium ruthenate (Y + Ru) and the Co^{2+} doped variant (Y + Ru + Co) exhibited similar lamellar structures in the scanning electron microscopy (SEM) images, and only the metallic Ru characteristic peaks could be observed from X-ray diffraction (XRD) patterns in Fig. S2. The similar initial states of precursors were conducive to eliminating the interferences in evaluating the effects of component interactions on thermal activation. Consequently, we further applied various thermal treatment processes to investigate the effects of Co addition.

Fig. 1a shows the crystalline structures of Y + Ru + Co and Y + Ru precursors after calcination. It was found that the pyrochlore phase (*Fd*$\bar{3}$*m*, JCPDS NO.28-1456) could be successfully formed with Co incorporation following a 1-hour heat treatment at 800 °C (the obtained sample was denoted as $Y_2Ru_{2-2x}Co_{2x}O_{7-\delta}$, the elemental composition from inductively coupled plasma is listed in Table S1), without other detectable crystal phases. In contrast, the single pyrochlore phase could not be obtained from the Y + Ru precursors with the same thermal treatment or even after 148 hours at 800 °C despite the existence of pyrochlore formation. For comparative purposes, the single-phase $Y_2Ru_2O_{7-\delta}$ (YRO) reference was prepared by 1 hour calcination at 1000 °C, as shown in Fig. S3.

Unlike our previous reports on the thermodynamic-accelerated formation of ruthenate,[25] which was prepared at a lower temperature (600 °C) than the close-to-equilibrium transition temperature (approximately 800 °C), the rapid kinetics appears to be the origin of the accelerated pyrochlore formation, the morphology of which at 800 °C was very close to that of the YRO reference at 1000 °C or the Y + Ru precursor at 800 °C for 148 hours (as shown in Fig. S4). The primary difference between $Y_2Ru_{1.6}Co_{0.4}O_{7-\delta}$ and YRO was the higher-angle shifted diffraction peaks of $Y_2Ru_{1.6}Co_{0.4}O_{7-\delta}$ compared to those of YRO, which should be attributed to the small ionic radius of Co substitutions.[26,27] The lattice parameter of $Y_2Ru_{1.6}Co_{0.4}O_{7-\delta}$ obtained by Rietveld refinement (Tables S2 and S3) was 10.1300 Å, which was smaller than that of YRO (10.1826 Å).

To investigate the efficiency of rapid phase transformation accelerated by the Co component, attempts were made to synthesize the $Y_2Ru_{2-2x}Co_{2x}O_{7-\delta}$ samples with different Co contents (x being from 0.5% to 50%). With the increase in Co content, the calcined samples showed the gradual disappearance of the RuO_2 phase, accompanied by the formation of a pyrochlore phase from the Y_2O_3 skeletons (Fig. S5). When the x value exceeded 30%, the Co_3O_4 phase was generated, indicating that the cobalt substitution within the pyrochlore structure had reached oversaturation. By quantitatively analyzing the

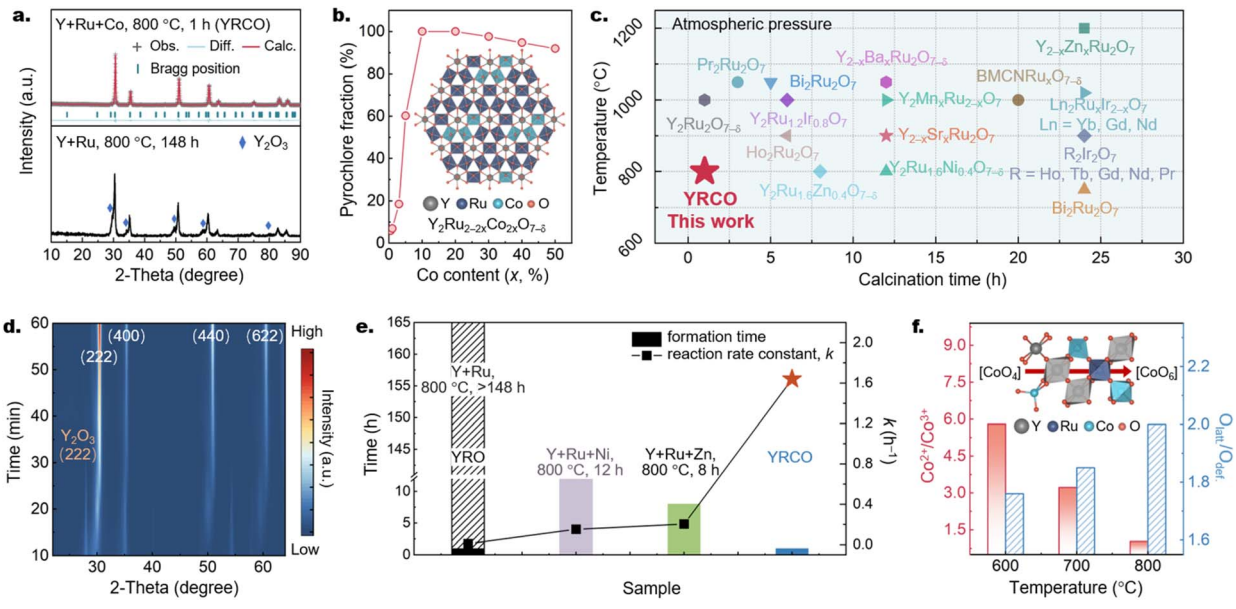

Fig. 1 (a) XRD patterns of the precursors with different calcination temperatures and times. (b) Pyrochlore fraction of YRCO with different Co contents. (c) The synthesis conditions of YRCO in this work compared with those of the reported ruthenate pyrochlores. (d) *In situ* XRD patterns of the Y + Ru + Co precursors at 800 °C. (e) The formation time of ruthenate pyrochlores with Ni, Zn, and Co substitutions at 800 °C, compared with the Y + Ru precursor. (f) $O_{latt.}/O_{def.}$ and Co^{2+}/Co^{3+} ratios of the Y + Ru + Co precursors at 600 °C, 700 °C, and 800 °C.

areas of the corresponding characteristic peak, a quantitative evaluation of the pyrochlore-phase content is listed in Fig. 1b. It was demonstrated that the addition of 5% cobalt was sufficient to enable the degree of pyrochlore formation to reach 60%.

The $Y_2Ru_{2-2x}Co_{2x}O_{7-\delta}$ samples with varying Co content were also evaluated by the electrochemical testing, where it was found that the sample exhibited optimal electrocatalytic activity when $x = 20\%$ (Fig. S6), and hence, $Y_2Ru_{1.6}Co_{0.4}O_{7-\delta}$ was selected as the representative sample (hereafter referred to as YRCO) for further characterization and discussion. We conducted a detailed comparison of the calcination time and temperature for YRCO with those reported in other studies. The acceleration strategy employing Co addition, as demonstrated in this study, was validated as a highly effective approach, particularly in reducing preparation time (Fig. 1c and Table S4).

To quantitatively analyze the effect of Co addition on the phase transformation process, *in situ* XRD was employed to characterize the structural evolution of products during phase formation (as shown in Fig. 1d and S7a). The mass fraction of the pyrochlore structure in the material was calculated *via* quantitative analysis of the XRD characteristic peak areas, and the classical Kolmogorov–Johnson–Mehl–Avrami (KJMA) equation[28] was used to fit the phase transformation kinetics:

$$X = 1 - \exp\{-[k(t - t_0)]^n\} \quad (1)$$

where X is the actual transformed fraction, $n = 3g + 1$ is the Avrami exponent particularized for three dimensional growth and the constant nucleation rate, g is the growing exponent, t is the induction time, and k is the reaction rate constant. The results indicated that the addition of Co significantly increased the Avrami exponent, with a fitted value of $n = 2.669$, as shown in Fig. 1e and S8. The growth exponent g was derived as 0.556, suggesting that the phase transformation process exhibits characteristics between diffusion-controlled decelerated growth ($g = 0.5$) and interface-controlled growth ($g = 1.0$).[29] For the Y + Ru precursor, $g = 0.131$, indicating that the sample follows a strongly decelerated diffusion-controlled growth mechanism, with substantially higher diffusion resistance compared to the Y + Ru + Co precursor. Furthermore, the fitted k of the Y + Ru + Co precursor (1.64 h^{-1}) was 164 times that of the Y + Ru precursor (0.010 h^{-1}). These results fully demonstrate that Co addition can significantly accelerate the kinetic diffusion behavior during the phase transformation process, thereby greatly promoting phase formation.

The analysis of specificity and universality of the Co-induced acceleration was further evaluated by using an equimolar amount of the other two small-sized transition-metal ions, Ni^{2+} or Zn^{2+}, as substitutions for the preparation of ruthenate pyrochlores (Fig. 1e, S7 and S8). These two substitutions also exhibited the acceleration effect for pyrochlore phase transformation (Zn: *ca.* 8 h at 800 °C; Ni: *ca.* 12 h at 800 °C). However, their efficiencies were inferior to that of the Co-substitution approach: the Zn-doped sample had $g = 0.318$ and $k = 0.193$ h^{-1}, while the Ni-based sample had $g = 0.195$ and $k = 0.152$ h^{-1}. Unlike Zn^{2+} (adopting a tetrahedral configuration) and $Ni^{2+/3+}$ (both showing octahedral configurations), Co cations typically display distinct coordination geometries depending on their oxidation states. This suggests that in addition to the small ionic size and low oxygen coordination number, cobalt also has a stabilizing effect with 6 coordination, which might be another key factor contributing to its outstanding acceleration performance.

We further attempted to investigate the variations during the process of phase transformation (from 600 °C to 800 °C, Fig. S9) induced by cobalt acceleration. X-ray photoelectron spectroscopy (XPS) was applied to analyze the chemical state of the elements. As shown in Fig. S10, the O 1s peak was deconvoluted into four peaks located at 529.5, 531.3, 532.2, and 533.5 eV, corresponding to lattice oxygen ($O_{latt.}$, at 529.5 eV), defective oxygen ($O_{def.}$, at 531.3 eV), surface adsorbed hydroxyl group (OH_{ads}, at 532.2 eV), and adsorbed water (H_2O_{ads}, at 533.5 eV), respectively.[30,31] The ratio of $O_{latt.}/O_{def.}$ was directly correlated with the formation of pyrochlore crystals. It was found that the ratio of $O_{latt.}/O_{def.}$ increased as the calcination temperature increased (Fig. 1f and Table S5), which was consistent with the XRD results. In addition, both of the Co^{2+} species (located at $2p_{3/2}$, 780.9 eV; $2p_{1/2}$, 796.9 eV; the corresponding satellites at 788.4 and 804.1 eV, respectively) and Co^{3+} species (located at $2p_{3/2}$, 779.6 eV; $2p_{1/2}$, 795.2 eV; the corresponding satellites at 786.6 and 802.4 eV, respectively) were observed in the high-resolution Co 2p spectra (Fig. S11 and Table S6). The Co^{3+} species usually exhibits six-fold coordination within octahedra such as $[CoO_6]$, while Co^{2+} usually exhibits four-fold coordination in tetrahedra, leading to an inherent oxygen deficiency.[16,32,33] Along with the formation of pyrochlore crystals, the decreased ratio of Co^{2+}/Co^{3+} indicated a gradual transformation of $[CoO_4]$ tetrahedra into $[CoO_6]$ octahedra, where the initial oxygen-deficit state could provide the oxygen vacancies for the accelerated diffusion of phase transformation, and at a later stage the generated $[CoO_6]$ octahedra were well-matched to substitute the B-site of $[RuO_6]$ and rapidly stabilize the pyrochlore phase.

To observe the morphologies and crystalline structure of YRCO in detail, transmission electron microscopy (TEM) was carried out. Similar to the observation in the SEM images, YRCO displayed the morphology of the significantly dispersed particles, which were distinguished from their precursors (Fig. 2a and S12). On the other hand, the Y + Ru precursors subjected to the same thermal treatment (800 °C for 1 h) exhibited a state similar to that of the corresponding precursor. With the increased content of the pyrochlore phase (Y + Ru, 800 °C, 148 h; Y + Ru, 1000 °C, 1 h), the dispersed particles came out as a result of mass diffusion (Fig. S13). This macroscopic phenomenon, which exhibits a similar crystal structure and morphology, is consistent with the accelerated diffusion behavior in kinetics rather than the thermodynamic effect. High-angle annular dark-field scanning transmission electron microscopy (HAADF-STEM) was further utilized to systematically assess the atomic arrangement in YRCO (Fig. 2b and S14). It showed a magnified lattice image with a crystal plane spacing of 0.298 nm corresponding to the (222) crystal plane of the pyrochlore structure, which was highly matched with the atomic position distributed in the crystal model.

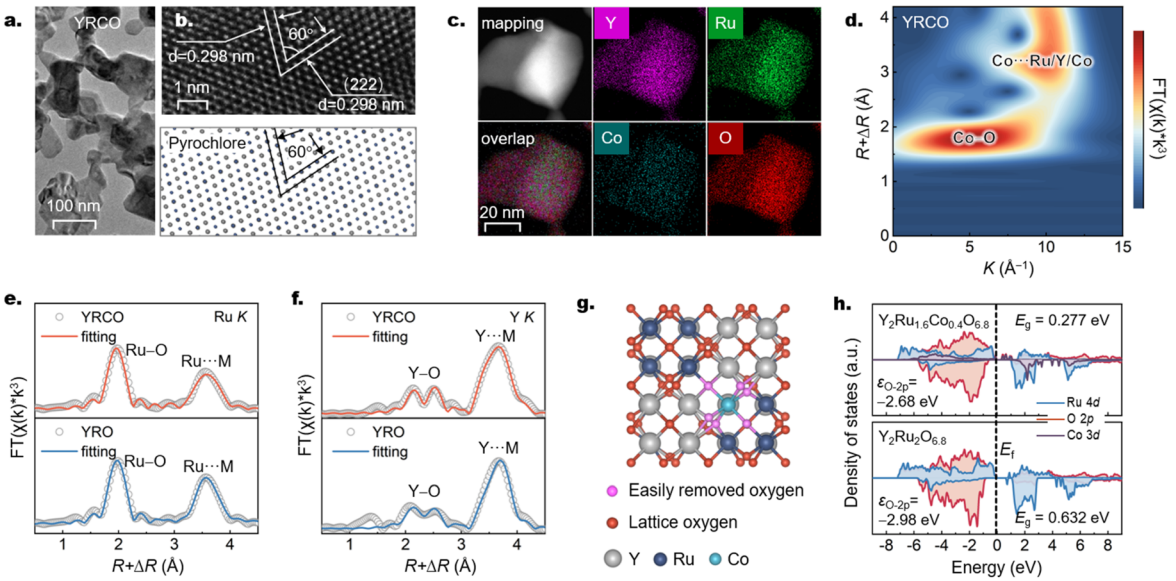

Fig. 2 (a) TEM image of Y + Ru + Co, 800 °C, 1 h (*i.e.*, YRCO). (b) HAADF-STEM image (top) and the mirrored modules (bottom) of YRCO. (c) EDX elemental mapping images of YRCO. (d) Morlet wavelet transform of Co K-edge EXAFS spectra of YRCO. (e) Ru K-edge and (f) Y K-edge EXAFS spectra of YRCO and YRO. (g) Illustration of the possible removed oxygen in YRCO; the actual structure will be more complex than that represented. (h) Partial density of states for $Y_2Ru_{1.6}Co_{0.4}O_{6.8}$ and $Y_2Ru_2O_{6.8}$.

In spite of the highly ordered atom arrangements observed in the pyrochlore phase, the element distribution was further analyzed by using energy dispersive X-ray (EDX) spectroscopy to verify whether the element segregation happened (Fig. 2c). The results confirmed that element Co was successfully integrated into the pyrochlore lattice, with all of the Y, Ru, Co, and O elements exhibiting uniform distribution. The detailed electronic structures of metal components were characterized by X-ray absorption near-edge structure spectroscopy (XANES). As depicted in the Co K-edge XANES spectra (Fig. S15a), the Co valence state in YRCO was calculated from the scaling linear relationship determined by the adsorption energies (E_0) of Co foil, CoO, and Co_3O_4 references with their nominal valence states (0, +2, and +2.67, respectively, Fig. S15b). The cobalt oxidation state was comprehensively determined to be +2.83, indicating that approximately 83% of the cobalt ions exist in the Co^{3+} state (Fig. S15c).

To elucidate the neighboring environment of Co in the first and second coordination shells, we conducted a Morlet wavelet transform analysis on the Co K-edge extended X-ray absorption fine structure spectroscopy (EXAFS) spectra of YRCO (Fig. 2d). There were two distinct lobes at R values of approximately 1.90 Å and 3.50 Å, attributed to the Co–O and Co···Ru/Y/Co bonds in the first and second coordination shells, respectively. Compared with the Co foil, CoO, and Co_3O_4 references as shown in Fig. S16, the analogous Co–O bond lobes to those of Co_3O_4 demonstrated the predominance of [CoO_6] octahedra in YRCO, but the Co···Ru/Y/Co bonds in the second shell were much longer than the Co···Co bonds in Co_3O_4 (located at around 3.45 Å and 2.96 Å) or CoO (located at around 3.25 Å). Considering the significantly smaller cation size of Co compared to Y,[34] the Co atoms within the [CoO_6] configuration mainly substituted into the B site of pyrochlore mostly due to the driving force of crystal fields.

Compared with the distance of Co···Ru/Y/Co, distinct peaks at approximately 3.60 Å were observed in both Ru K-edge and Y K-edge EXAFS spectra, corresponding to the Ru···Ru/Y/Co and Y···Ru/Y/Co paths in the second shell (Fig. 2e and f), which constitute the primary structural framework in pyrochlores. Additionally, there was no obvious difference between YRCO and YRO on the signal peak at a radial distance of 1.98 Å (the Ru–O bond within the first coordination shell of the [RuO_6] octahedra) in the Ru K-edge EXAFS spectra, or the two minor peaks at 2.23 Å (corresponding to the Y–O–(M_A)) and 2.40 Å (Y–O–(M_B)) in the Y K-edge EXAFS spectra. Analogously, the valence states of Ru and Y also had no significant difference between YRCO and YRO (Fig. S17). Thus, the EXAFS curves were fitted, and the fitting parameters are listed in Tables S7 and S8. YRCO exhibited a higher Ru–O coordination number of 5.9 ± 0.5 compared to YRO (5.6 ± 0.5). However, the difference was not significant for the Y–O coordination (5.9 ± 0.7 in YRCO and 5.8 ± 0.9 in YRO). It seemed that the oxygen coordination was increased around Ru on the B-site rather than the A-site in YRCO. However, the O 1s XPS spectra (Fig. S18 and Table S5) showed an increase of $O_{def.}$ in YRCO (26.2%) compared to YRO (24.2%). Furthermore, with the increase in Co content, the concentration of oxygen vacancies gradually increases and subsequently tends to stabilize, as shown in Fig. S10b. In addition, the increase in O_v content in YRCO was also consistent with the molecular dynamics (MD) calculation results (Fig. S19 and Table S9, more calculation details are included in the SI), which will facilitate the LOM process in the OER.[35] Combined with the high Ru–O coordination number, the overall increase of oxygen vacancies should be attributed to the

oxygen deficiency neighboring the Co cations at the B-site. Here, the oxygen coordinated with Co can be captured by the nearby Ru leading to an increased Ru–O coordination. The possible atomic structure in YRCO is shown in Fig. 2g and Fig. S20. Density functional theory (DFT) calculations were performed to investigate the electronic structures of $Y_2Ru_{1.6}Co_{0.4}O_{6.8}$ and $Y_2Ru_2O_{6.8}$, whose structures are illustrated in Fig. S21. The partial density of states in Fig. 2h shows the upshifted O 2p band center in $Y_2Ru_{1.6}Co_{0.4}O_{6.8}$ (from −2.98 eV to −2.68 eV), indicating that oxygen in this compound is more prone to act as an active site to initiate the LOM pathway.[5,36] Meanwhile, with a smaller band gap of 0.277 eV compared to 0.632 eV, $Y_2Ru_{1.6}Co_{0.4}O_{6.8}$ exhibits superior electrical conductivity.

We evaluated the electrochemical OER activities of YRCO, compared with YRO, commercial RuO_2, and IrO_2, in either 0.1 M $HClO_4$ or 1.0 M KOH electrolyte. In the acidic electrolyte, the *iR*-compensated linear sweep voltammetry (LSV) curves (Fig. 3a) showed that YRCO only required a small overpotential of 214 mV to reach the benchmark current density of 10 mA cm^{-2}, which was superior to those of YRO (267 mV), IrO_2 (297 mV), and RuO_2 (301 mV). As expected, the enhanced OER activity of YRCO was also detected under alkaline conditions (Fig. 3b) and neutral conditions (Fig. S22). The smaller Tafel slopes in Fig. S23 also indicate the significantly accelerated OER kinetics of YRCO compared to the other samples in both acid (48.5 mV dec^{-1}) and alkali (50.5 mV dec^{-1}), where the rate-determining step should be the second dissociation of the adsorbed hydroxyl in the lattice oxygen participation mechanism.[31,37] The enhanced OER kinetics for YRCO was further confirmed by the electrochemical impedance spectroscopy (EIS) measurements (Fig. 3c). Only one potential-dependent low-frequency semicircle was observed for each pyrochlore sample, which was related to the charge transfer process and double layer capacitance.[38] The corresponding equivalent electrical circuit consisted of three components: solution resistance (R_{sol}), charge transfer resistance (R_{ct}), and double layer capacitance (C_{dl}). At an overpotential of 250 mV, YRCO exhibited a much smaller R_{ct} than YRO, indicating that electrons were easily transferred through the electrode/electrolyte interface (Table S10). The significant disparity in R_{ct} values between acidic and alkaline conditions can be attributed to the distinct ion mobility and conductivity characteristics of H^+ and OH^- ions at varying concentrations.[39]

In order to further verify the enhanced OER activity, we investigated the pH-dependence behavior of these rutheniumbased pyrochlores across various pH levels to measure their unsynchronized deprotonation process (Fig. S24). As shown in Fig. 3d, YRCO exhibits a higher pH dependence coefficient (−0.76 under acidic conditions and 0.75 under alkaline conditions) compared to those of YRO, indicating a more pronounced LOM pathway in either acid or alkali.[40] The pronounced LOM facilitates direct O–O bond formation by coupling between lattice oxygen and surface-adsorbed species and bypassing the *OOH intermediates. As a result, it breaks the scaling relationship limitation and significantly enhances the catalytic activity.[41] Therefore, YRCO showed a competitive activity compared with the several OER catalysts reported in recent years (Table S11).

Although the enhanced LOM process could increase the OER activity, the corresponding stability is still a challenge due to the highly possible loss of lattice oxygen. Therefore, we applied

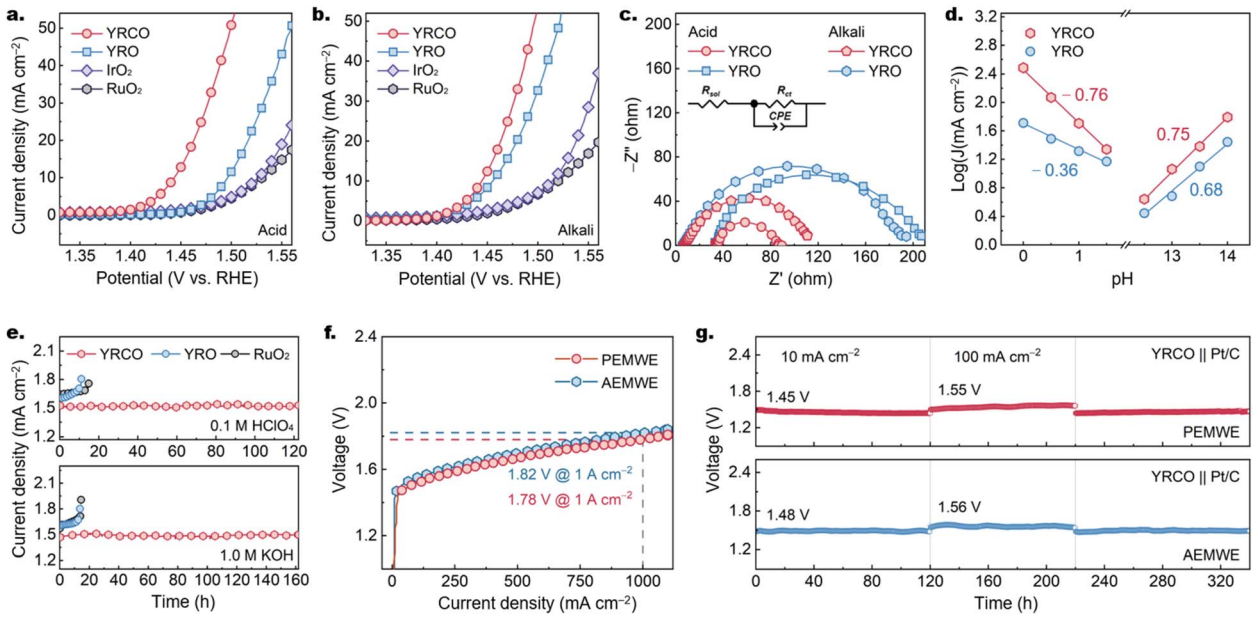

Fig. 3 *IR*-compensated LSV curves of YRCO, YRO, commercial RuO_2, and commercial IrO_2 recorded at a scan rate of 10 mV s^{-1} in (a) 0.1 M $HClO_4$ and (b) 1.0 M KOH solution. (c) Nyquist plots of YRCO and YRO at an overpotential of 250 mV in acid and alkali. (d) The relationship between the current density of YRCO and YRO at an overpotential of 300 mV and the pH value of the electrolyte. (e) Chronopotentiometry of YRO and YRCO in 0.1 M $HClO_4$ and 1.0 M KOH solution. (f) Voltage–current density curves and (g) the typical galvanostatic curves of YRCO-derived PEMWE and AEMWE, where Pt/C was used as cathodes for the overall water electrolysis.

chronopotentiometric measurements to evaluate the stability of YRCO and YRO. Compared to YRO, YRCO maintained a lower and more stable potential during continuous operation at a current density of 10 mA cm^{-2} (Fig. 3e). The potential for YRO was raised above 1.8 V (*vs.* RHE) within 15 hours, while YRCO exhibits stability for up to 120 h in 0.1 M $HClO_4$ solution and 160 h in 1.0 M KOH solution. Meanwhile, the ion concentration in the electrolyte was measured within the first 12 hours of the lifespan test, and the results are provided in Fig. S25 and Table S12. Catalyst surface reconstruction in the initial stage induces a rapid increase in ion concentration, which then stabilizes.[42] The Y dissolution amount in the YRCO electrolyte is only 1/8 that of YRO, and the Ru dissolution amount (0.91 mg L^{-1}) is significantly lower than that in YRO (2.35 mg L^{-1}). The high stability of YRCO was also observed in the proton exchange membrane water electrolyzer (PEMWE) and anion exchange membrane water electrolyzer (AEMWE) testing. The device performance of these pyrochlore samples was evaluated when used as the active anode with 20 wt% Pt/C as a cathode, for the overall water electrolysis. As shown in Fig. 3f, the voltage–current density curves indicate that the voltage required for the PEMWE and AEMWE to reach a current density of 1 A cm^{-2} is 1.78 V and 1.82 V, respectively. The long-term device operation also reconfirmed that at alternating current densities of 10 mA cm^{-2} and 100 mA cm^{-2}, YRCO exhibited excellent stability of more than 340 hours both in the PEMWE and AEMWE (Fig. 3g).

The unexpected long service life of the LOM-pronounced OER electrocatalysts motivated us to deeply investigate the origin of YRCO stability. Hence, following the chronopotentiometric measurements conducted in an acidic environment, the YRCO and YRO catalysts were further characterized. As illustrated in Fig. 4a, YRCO preserved its conductor properties at end-of-life (EoL), characterized by charge carrier mobility rather than carrier concentration dominating the conductivity, exhibiting a gradual increase in resistivity with rising temperature. In contrast, YRO exhibited insulator behavior. The great change in electrical properties is due to the slight atom variation in the strongly correlated electron systems of pyrochlores and further triggers the metal–insulator (M–I) deactivation, one kind of special electrochemical attenuation for these complex ruthenate compounds that was reported in our previous work.[10] The unexpectedly long catalytic lifetime of YRCO indicates that the atoms within its lattice are significantly more stable than those in YRO.

As a more important feature, the oxygen states of YRCO at EoL were further investigated and compared with those at the initial state. Electron paramagnetic resonance (EPR) spectra (Fig. S26) showed that the oxygen vacancy in YRCO was increased from 2.526×10^{13} to 4.296×10^{13} spins per g, which was higher than that of YRO (from 1.396×10^{13} to 2.514×10^{13} spins per g). This was foreseeable for YRCO with the stronger LOM pathway. However, the Rietveld refinement of XRD patterns (Fig. 4b, S27 and Table S3) revealed that the change in lattice parameters of YRCO (only $\Delta a = 0.0027$ Å) was much smaller than that of YRO ($\Delta a = 0.0391$ Å) after the reaction. To reconfirm this result, we derived the supercell structure diagram from the aforementioned MD calculations. It was noteworthy that there was a smaller impact of the O_v generation on the overall structure of $Y_2Ru_{1.6}Co_{0.4}O_{7-\delta}$ compared to $Y_2Ru_2O_{7-\delta}$, even if the oversaturated O_v concentration was artificially constructed (Fig. 4c and S28). Meanwhile, $Y_2Ru_{1.6}$-$Co_{0.4}O_{7-\delta}$ showed much smaller changes in lattice parameters than $Y_2Ru_2O_{7-\delta}$, and its band gap also remained nearly unchanged compared with $Y_2Ru_2O_{7-\delta}$ (Fig. S29). The great relief of lattice field variations demonstrated that the Co substitution played an important role in stabilizing atom arrangement in pyrochlore and thereby stabilizing the conductive state.

Therefore, the elemental analysis was further conducted for the YRCO sample at EoL. The EDX mapping and TEM images after the stability assessment demonstrated that the elements of Y, Ru, Co, and O also exhibited the stability of atomic dispersion within YRCO, the nanocrystal structure of which was retained (Fig. S30 and S31). Despite this, XPS measurement showed the surficial Co species were largely reduced due to the metal leaching that occurred during the OER process (Fig. S32). Thus, electron energy loss spectroscopy (EELS) was further used to detect the bulk chemical state of Ru and Co in YRCO. As shown in Fig. S33, both the Co L edge and the Ru M edge exhibited a negative shift, indicating the decrease of their chemical valence states,[43,44] which was consistent with the Co K-edge XANES results (Fig. S34). This should be attributed to the produced O_v during the OER.

To study the reasons why O_v in YRO and YRCO has different effects on their respective lattices, first, we calculated the charges of O_v adjacent to Co and Ru. The charge section diagram (Fig. 4d) shows that, compared with Ru, the charge of O_v near Co has significantly decreased. We guess this is because the O_v generated electron could be easily accepted by Co^{3+}, which would become Co^{2+}. In the synergistic effect associated with the expansion of low valence ions and contraction of atom losses, the lattice field will be stabilized.[45,46] Furthermore, we carried out MD simulations on the B-site tetramer units, including $[RuO_6]_3$–$[CoO_6]$ and $[RuO_6]_4$, within the pyrochlore structure. The energy changes ($|\Delta E|$) and geometric transformations were calculated, when each one type of oxygen atom was removed. The O_v near Co exhibited higher thermodynamic stability with a larger $|\Delta E|$ value than those near Ru (Fig. S35). This demonstrated that the generated O_v was beneficial to be stabilized near Co in the LOM pathway. This stabilization was analyzed by the geometric transformations during the kinetic process. As shown in Fig. 4e and S36, the oxygen-deficit $[CoO_5]$ octahedra would be transformed into the $[CoO_4]$ tetrahedral configuration, when O_v was located at either site 1 or site 2. Comparatively, the configuration of the $[RuO_5]$ polyhedron in $[RuO_6]_3$–$[RuO_5]$ would become a $[RuO_4]$ planar tetragonal structure or $[RuO_5]$ quadrangular pyramid structure, which originated from their parent $[RuO_6]$. Finally, we analyzed Co K-edge EXAFS spectra of the catalyst before and after the OER testing, as shown in Fig. 4f and g. The signal near 2.0 Å originated from the Co–O path of the first shell, and the signal in the 3.0 Å to 4.0 Å range originated from the Co⋯Ru/Y/Co path. After the reaction, the peak intensity related to the Co–O bond significantly decreased. The fitting results indicated that the coordination number of the Co–O bond decreased from 5.6 ± 0.6 to 4.0 ± 0.7, confirming the structural transformation of

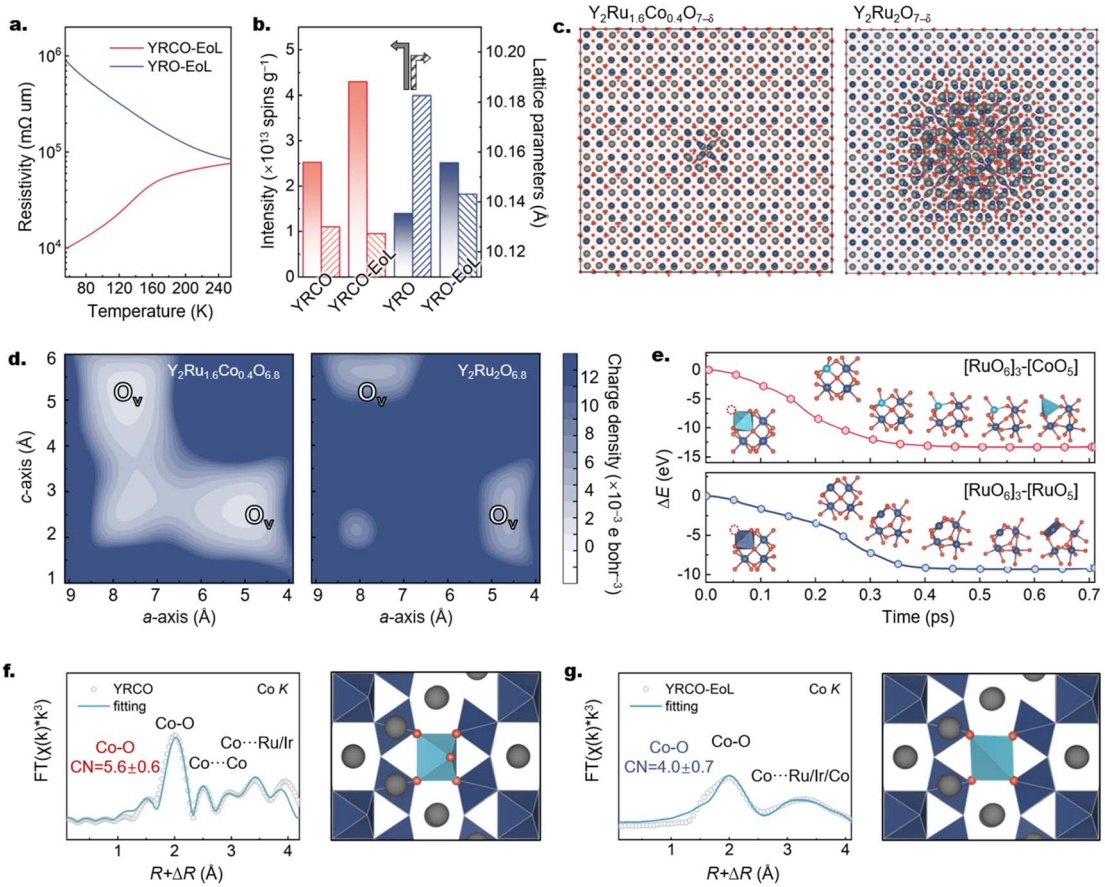

Fig. 4 (a) Temperature-dependent resistivity of YRCO and YRO at EoL. (b) The oxygen vacancy concentration derived from EPR spectra and the lattice parameters obtained *via* Rietveld refinement for YRCO and YRO. (c) The MD-simulated 5 × 5 × 5 supercell models of $Y_2Ru_{1.6}Co_{0.4}O_{7-\delta}$ and $Y_2Ru_2O_{7-\delta}$ with 0.43‰ oxygen vacancies. (d) Space charge section obtained using DFT calculations of $Y_2Ru_{1.6}Co_{0.4}O_{6.8}$ and $Y_2Ru_2O_{6.8}$. (e) MD-simulated energy variation and the corresponding structural transformation processes of B-site clusters with an oxygen atom deficiency. (f) The Co K-edge EXAFS spectra of YRCO and the corresponding Co polyhedral configurations. (g) The Co K-edge EXAFS spectra of YRCO at EoL and the corresponding Co polyhedral configurations.

Co from the high-coordination $[CoO_6]$ octahedron to the low-coordination $[CoO_4]$ tetrahedron (Tables S13 and S14). This local tetrahedral coordination is expected to effectively mitigate the impact of oxygen vacancies on the rigid lattice distortion of the pyrochlore structure, thereby suppressing the M-I deactivation and endowing YRCO with a prolonged catalytic lifetime.

Conclusions

In summary, this work reports a Co-mediated strategy to regulate oxygen vacancies, achieving dual breakthroughs in ruthenate pyrochlore synthesis control and OER performance enhancement. The significant acceleration of the phase transition by 164 times (based on the reaction rate constant k) was attributed to the enhanced atomic diffusion from the natural "oxygen vacancies" of the $[CoO_4]$ tetrahedra and the rapid stabilization of the well-matched $[CoO_6]$ octahedra at the B site in pyrochlores. Comprehensive characterization and theoretical calculations confirm that Co substitution enriches O_v around the B-site, which boosts OER activity through the LOM pathway. Meanwhile, YRCO also exhibited a high electrochemical stability due to the transformation of $[CoO_6]$ into $[CoO_4]$. This transition alleviates lattice field distortions, suppresses metal-insulator transition, and thereby greatly enhances the service life of this multicomponent electrocatalyst in either the electrochemical testing or the PEM/AEM electrolyzers for water electrolysis. We believe that these findings not only provide novel insights into the regulatory mechanism of oxygen vacancies in the materials, but also establish a universal synthetic approach for functional but high-temperature materials, such as perovskites, ilmenites, and garnets.

Author contributions

Z. P. Z. conceived and directed the project. F. W. contributed to direction guidance and manuscript revision. Y. Z. H. performed most of the experiments, analyzed the results, and wrote the manuscript. T. T. L. contributed to data processing and manuscript revision. Q. R. Z. contributed to data processing. All authors have given approval to the final version of the manuscript.

Conflicts of interest

The authors declare no conflict of interest.

Data availability

All data needed to evaluate the conclusions in the paper are present in the paper and/or the supplementary information (SI). Supplementary information: additional experimental details and characterization data, including XRD, XPS, SEM, and TEM. See DOI: https://doi.org/10.1039/d5sc09343k.

Acknowledgements

This work was supported by the National Key R&D Program of China (2022YFE0110400), the National Natural Science Foundation of China (52173245, U24A20526, 52122207, 52130206, and 52221006), the China National Petroleum Corporation Innovation Consortium Project (H20230769), and the Fundamental Research Funds for the Central Universities (JD2520 and CLYY2022). The authors are grateful to the beamline 1W1B station of the Beijing Synchrotron Radiation Facility for the XAFS tests.

Notes and references

1 X. Qian, L. Chen, L. Yin, Z. Liu, S. Pei, F. Li, G. Hou, S. Chen, L. Song, K. H. Thebo, H. M. Cheng and W. Ren, $CdPS_3$ Nanosheets-based Membrane with High Proton Conductivity Enabled by Cd Vacancies, *Science*, 2020, **370**, 596–600.

2 P. Nukala, M. Ahmadi, Y. Wei, S. D. Graaf, E. Stylianidis, T. Chakrabortty, S. Matzen, H. W. Zandbergen, A. Björling, D. Mannix, D. Carbone, B. Kooi and B. Noheda, Reversible Oxygen Migration and Phase Transitions in Hafnia-Based Ferroelectric Devices, *Science*, 2021, **372**, 630–635.

3 Z. Luo, W. Gao and Q. Jiang, Determinants of Vacancy Formation and Migration in High-entropy Alloys, *Sci. Adv.*, 2025, **11**, eadr4697.

4 T. Zhang, H. F. Zhao, Z. J. Chen, Q. Yang, N. Gao, L. Li, N. Luo, J. Zheng, S. D. Bao, J. Peng, X. Peng, X. W. Liu and H. B. Yu, High-Entropy Alloy Enables Multi-Path Electron Synergism and Lattice Oxygen Activation for Enhanced Oxygen Evolution Activity, *Nat. Commun.*, 2025, **16**, 3327.

5 X. Wang, S. Xi, P. Huang, Y. Du, H. Zhong, Q. Wang, A. Borgna, Y. W. Zhang, Z. Wang, H. Wang, Z. G. Yu, W. S. V. Lee and J. Xue, Pivotal Role of Reversible NiO_6 Geometric Conversion in Oxygen Evolution, *Nature*, 2022, **611**, 702–708.

6 J. J. Song, C. Wei, Z. F. Huang, C. T. Liu, L. Zeng, X. Wang and Z. C. J. Xu, A Review on Fundamentals for Designing Oxygen Evolution Electrocatalysts, *Chem. Soc. Rev.*, 2020, **49**, 2196–2214.

7 R. R. Rao, S. Corby, A. Bucci, M. Garcia-Tecedor, C. A. Mesa, J. Rossmeisl, S. Giménez, J. Lloret-Fillol, I. E. L. Stephens and J. R. Durrant, Spectroelectrochemical Analysis of the Water Oxidation Mechanism on Doped Nickel Oxides, *J. Am. Chem. Soc.*, 2022, **144**, 7622–7633.

8 Z. Li, J. Yang, Z. Chen, C. Zheng, L. Q. Wei, Y. Yan, H. Hu, M. Wu and Z. Hu, V "Bridged" Co-O to Eliminate Charge Transfer Barriers and Drive Lattice Oxygen Oxidation during Water-Splitting, *Adv. Funct. Mater.*, 2021, **31**, 2008822.

9 S. Zhao, D. Kang, Y. Liu, Y. Wen, X. Xie, H. Yi and X. Tang, Spontaneous Formation of Asymmetric Oxygen Vacancies in Transition-Metal-Doped CeO_2 Nanorods with Improved Activity for Carbonyl Sulfide Hydrolysis, *ACS Catal.*, 2020, **10**, 11739–11750.

10 T. Liu, H. Guo, Q. Zhang, M. Fujishige, M. Endo, Z. Zhang and F. Wang, Insulator-Transition-Induced Degradation of Pyrochlore Ruthenates in Electrocatalytic Oxygen Evolution and Stabilization through Doping, *Angew. Chem., Int. Ed.*, 2024, **63**, e202412139.

11 G. G. Guzmán-Verri, R. T. Brierley and P. B. Littlewood, Cooperative Elastic Fluctuations Provide Tuning of The Metal–Insulator Transition, *Nature*, 2019, **576**, 429–432.

12 J. H. Lee, S. Lee, T. Kim, H. Ahn, G. Y. Jang, K. H. Kim, Y. J. Cho, K. Zhang, J. S. Park and J. H. Park, Interfacial α-$FAPbI_3$ Phase Stabilization by Reducing Oxygen Vacancies in SnO_{2-x}, *Joule*, 2023, **7**, 380–397.

13 Y. Zhang, Y. Zhou, D. Sun, Y. Nie, D. Wu, L. Ban, B. Tang, S. Yang, H. Li, T. Ma and H. Zhang, CeO_2-based Functional Materials: Advancing Photo and Electro-driven Catalysis for Environmental Remediation and Energy Conversion, *Coord. Chem. Rev.*, 2025, **527**, 216395.

14 Y. Sun, Q. Wang, Z. Geng, Z. Liu and R. Yang, Fabrication of Two-Dimensional 3d Transition Metal Oxides through Template Assisted Cations Hydrolysis Method, *Chem. Eng. J.*, 2021, **415**, 129044.

15 S. Sun, Y. Sun, Y. Zhou, S. Xi, X. Ren, B. Huang, H. Liao, L. P. Wang, Y. Du and Z. J. Xu, Shifting Oxygen Charge Towards Octahedral Metal: A Way to Promote Water Oxidation on Cobalt Spinel Oxides, *Angew. Chem., Int. Ed.*, 2019, **58**, 6042–6047.

16 L. Chong, G. Gao, J. Wen, H. Li, H. Xu, Z. Green, J. D. Sugar, A. J. Kropf, W. Xu, X. M. Lin, H. Xu, L. W. Wang and D. J. Liu, La- and Mn-doped Cobalt Spinel Oxygen Evolution Catalyst for Proton Exchange Membrane Electrolysis, *Science*, 2023, **380**, 609–616.

17 Y. Zhao, N. Dongfang, C. Huang, R. Erni, J. Li, H. Zhao, L. Pan, M. Iannuzzi and G. R. Patzke, Operando Monitoring of The Functional Role of Tetrahedral Cobalt Centers for The Oxygen Evolution Reaction, *Nat. Commun.*, 2025, **16**, 580.

18 J. Qi, Y. P. Lin, D. Chen, T. Zhou, W. Zhang and R. Cao, Autologous Cobalt Phosphates with Modulated Coordination Sites for Electrocatalytic Water Oxidation, *Angew. Chem., Int. Ed.*, 2020, **59**, 8917–8921.

19 J. Li, M. X. Guan, P. F. Nan, J. Wang, B. H. Ge, K. M. Qiao, H. R. Zhang, W. H. Liang, J. Z. Hao, H. B. Zhou, F. R. Shen, F. X. Liang, C. Zhang, M. Liu, S. Meng, T. Zhu, F. X. Hu, T. Wu, J. D. Guo, J. R. Sun and B. G. Shen, Topotactic Phase Transformations by Concerted Dual-ion

Migration of B-site Cation and Oxygen in Multivalent Cobaltite La-Sr-Co-O_x films, *Nano Energy*, 2020, **78**, 105215.

20 A. Bergmann, E. Martinez-Moreno, D. Teschner, P. Chernev, M. Gliech, J. F. de Araújo, T. Reier, H. Dau and P. Strasser, Reversible Amorphization and the Catalytically Active State of Crystalline Co_3O_4 during Oxygen Evolution, *Nat. Commun.*, 2015, **6**, 8625.

21 A. Navrotsky, C. Ma, K. Lilova and N. Birkner, Nanophase Transition Metal Oxides Show Large Thermodynamically Driven Shifts in Oxidation-Reduction Equilibria, *Science*, 2010, **330**, 199–201.

22 J. Kim, P. C. Shih, Y. Qin, Z. Al-Bardan, C. J. Sun and H. Yang, A Porous Pyrochlore $Y_2[Ru_{1.6}Y_{0.4}]O_{7-\delta}$ Electrocatalyst for Enhanced Performance towards the Oxygen Evolution Reaction in Acidic Media, *Angew. Chem., Int. Ed.*, 2018, **57**, 13877–13881.

23 T. Liu, H. Guo, Y. Chen, Z. Zhang and F. Wang, Role of MoO_x Surficial Modification in Enhancing the OER Performance of Ru-Pyrochlore, *Small*, 2023, **19**, 2206698.

24 X. Su, F. Fu, Y. Yan, G. Zheng, T. Liang, Q. Zhang, X. Cheng, D. Yang, H. Chi, X. Tang, Q. Zhang and C. Uher, Self-Propagating High-Temperature Synthesis for Compound Thermoelectrics and New Criterion for Combustion Processing, *Nat. Commun.*, 2014, **5**, 4908.

25 Q. Zhang, T. Liu, H. Guo, Y. Chen, Y. Di, Z. Zhang and F. Wang, Lead-Induced Microstrain in Synthesis and Manipulation of Porous Pyrochlore for Boosting Oxygen Evolution Reaction, *Adv. Funct. Mater.*, 2024, **34**, 2306176.

26 J. Kim, P. C. Shih, K. C. Tsao, Y. T. Pan, X. Yin, C. J. Sun and H. Yang, High-Performance Pyrochlore-Type Yttrium Ruthenate Electrocatalyst for Oxygen Evolution Reaction in Acidic Media, *J. Am. Chem. Soc.*, 2017, **139**, 12076–12083.

27 X. Ping, Y. Liu, L. Zheng, Y. Song, L. Guo, S. Chen and Z. Wei, Locking the Lattice Oxygen in RuO_2 to Stabilize Highly Active Ru Sites in Acidic Water Oxidation, *Nat. Commun.*, 2024, **15**, 2501.

28 G. Krainer, T. J. Welsh, J. A. Joseph, J. R. Espinosa, S. Wittmann, E. de Csilléry, A. Sridhar, Z. Toprakcioglu, G. Gudiškytė, M. A. Czekalska, W. E. Arter, J. Guillén-Boixet, T. M. Franzmann, S. Qamar, P. S. George-Hyslop, A. A. Hyman, R. Collepardo-Guevara, S. Alberti and T. P. J. Knowles, Reentrant Liquid Condensate Phase of Proteins is Stabilized by Hydrophobic and Non-ionic Interactions, *Nat. Commun.*, 2021, **12**, 1085.

29 R. Kitahara, R. Yamazaki, F. Ide, S. Li, Y. Shiramasa, N. Sasahara and T. Yoshizawa, Pressure-Jump Kinetics of Liquid–Liquid Phase Separation: Comparison of Two Different Condensed Phases of the RNA-Binding Protein, Fused in Sarcoma, *J. Am. Chem. Soc.*, 2021, **143**, 19697–19702.

30 Z. Li, C. Zhou, J. Hua, X. Hong, C. Sun, H. Li, X. Xu and L. Mai, Engineering Oxygen Vacancies in a Polysulfide-Blocking Layer with Enhanced Catalytic Ability, *Adv. Mater.*, 2020, **32**, 1907444.

31 S. Hao, M. Liu, J. Pan, X. Liu, X. Tan, N. Xu, Y. He, L. Lei and X. Zhang, Dopants Fixation of Ruthenium for Boosting Acidic Oxygen Evolution Stability and Activity, *Nat. Commun.*, 2020, **11**, 5368.

32 W. Zhu, F. Yao, K. J. Cheng, M. Zhao, C. J. Yang, C. L. Dong, Q. Hong, Q. Jiang, Z. Wang and H. Liang, Direct Dioxygen Radical Coupling Driven by Octahedral Ruthenium-Oxygen-Cobalt Collaborative Coordination for Acidic Oxygen Evolution Reaction, *J. Am. Chem. Soc.*, 2023, **145**, 17995–18006.

33 H. Zhou, H. Li, L. Wang, S. Chu, L. Liu, L. Liu, J. Qi, Z. Ren, A. Cai, Y. Hui, Y. Qin, L. Song, X. Qin, J. Shi, J. Hou, Y. Ding, J. Ma, S. Xu, X. Tao, L. Li, Q. Yang, B. Hu, X. Liu, L. Chen, J. Xiao and F. S. Xiao, Cobaltosilicate Zeolite beyond Platinum Catalysts for Propane Dehydrogenation, *Nat. Catal.*, 2025, **8**, 357–367.

34 L. Zhang, D. Hu, X. Li, Z. Liu, C. Hu, L. Wu, T. Li, D. Hreniak and J. Li, Effect of Y Substitution on the Microstructure, Magneto-optical, and Thermal Properties of $(Tb_{1-x}Y_x)_3Al_5O_{12}$ Transparent Ceramics, *J. Adv. Ceram.*, 2024, **13**, 529–538.

35 N. Han, S. Feng, Y. Liang, J. Wang, W. Zhang, X. Guo, Q. Ma, Q. Liu, W. Guo, Z. Zhou, S. Xie, K. Wan, Y. Jiang, A. Vlad, Y. Guo, E. M. Gaigneaux, C. Zhang, J. Fransaer and X. Zhang, Achieving Efficient Electrocatalytic Oxygen Evolution in Acidic Media on Yttrium Ruthenate Pyrochlore through Cobalt Incorporation, *Adv. Funct. Mater.*, 2023, **33**, 2208399.

36 Y. Zhu, H. A. Tahini, Z. Hu, Z. G. Chen, W. Zhou, A. C. Komarek, Q. Lin, H. J. Lin, C. T. Chen, Y. Zhong, M. T. Fernández-Díaz, S. C. Smith, H. Wang, M. Liu and Z. Shao, Boosting Oxygen Evolution Reaction by Creating Both Metal Ion and Lattice-Oxygen Active Sites in a Complex Oxide, *Adv. Mater.*, 2020, **32**, 1905025.

37 A. Grimaud, O. Diaz-Morales, B. Han, W. T. Hong, Y. L. Lee, L. Giordano, K. A. Stoerzinger, M. T. M. Koper and Y. Shao-Horn, Activate Lattice Oxygen Redox Reactions in Metal Oxides to Catalyse Oxygen Evolution, *Nat. Chem.*, 2018, **10**, 457–465.

38 M. Gaberšček, Understanding Li-based Battery Materials via Electrochemical Impedance Spectroscopy, *Nat. Commun.*, 2021, **12**, 6513.

39 L. An, C. Wei, M. Lu, H. Liu, Y. Chen, G. G. Scherer, A. C. Fisher, P. Xi, Z. J. Xu and C. H. Yan, Recent Development of Oxygen Evolution Electrocatalysts in Acidic Environment, *Adv. Mater.*, 2021, **33**, 2006328.

40 X. Wang, H. Zhong, S. Xi, W. S. V. Lee and J. Xue, Understanding of Oxygen Redox in the Oxygen Evolution Reaction, *Adv. Mater.*, 2022, **34**, 2107956.

41 Y. Pan, X. Xu, Y. Zhong, L. Ge, Y. Chen, J. P. M. Veder, D. Guan, R. O'Hayre, M. Li, G. Wang, H. Wang, W. Zhou and Z. Shao, Direct Evidence of Boosted Oxygen Evolution over Perovskite by Enhanced Lattice Oxygen Participation, *Nat. Commun.*, 2020, **11**, 2002.

42 H. Guo, Y. Huang, C. Long, C. Shao, F. Fang, Y. Yu, Z. Zhang and F. Wang, Lattice Distortion Engineering: Manipulation of Electrochemical Properties for Pyrochlore Ruthenates as Electrocatalysts in Water Splitting, *Small*, 2025, **21**, 2505222.

43 J. I. Deitz, P. K. Paul, R. Farshchi, D. Poplavskyy, J. Bailey, A. R. Arehart, D. W. McComb and T. J. Grassman, Direct Nanoscale Characterization of Deep Levels in $AgCuInGaSe_2$ Using Electron Energy-Loss Spectroscopy in the Scanning Transmission Electron Microscope, *Adv. Energy Mater.*, 2019, **9**, 1901612.

44 K. Jenkinson, M. C. Spadaro, V. Golovanova, T. Andreu, J. R. Morante, J. Arbiol and S. Bals, Direct Operando Visualization of Metal Support Interactions Induced by Hydrogen Spillover During CO_2 Hydrogenation, *Adv. Mater.*, 2023, **35**, 2306447.

45 A. X. B. Yong, L. O. Anderson, N. H. Perry and E. Ertekin, Effects of State Filling and Localization on Chemical Expansion in Praseodymium-Oxide Perovskites, *J. Mater. Chem. A*, 2023, **11**, 4045–4056.

46 D. Marrocchelli, S. R. Bishop, H. L. Tuller and B. Yildiz, Understanding Chemical Expansion in Non-Stoichiometric Oxides: Ceria and Zirconia Case Studies, *Adv. Funct. Mater.*, 2012, **22**, 1958–1965.